

# Chapter 13

## Recent Advances in Global Fracture Mechanics of Growth of Large Hydraulic Crack Systems in Gas or Oil Shale: A Review

Zdeněk P. Bažant and Viet T. Chau

**Abstract** This chapter reviews the recent progress toward computer simulation of the growth of vast systems of branched hydraulic cracks needed for the efficient extraction of gas or oil from shale strata. It is emphasized that, to achieve significant gas extraction, the spacing of parallel hydraulic cracks must be on the order of 0.1 m, which means that the fracturing of the entire fracking stage would require creating about a million vertical cracks. Another emphasized feature is that the viscous flow of fracking water along the hydraulic cracks must be combined with Darcy diffusion of a large amount of water into the pores and flaws in shale. The fracture mechanics on the global scale is handled by the crack band model with gradual postpeak softening and a localization limiter in the form of a material characteristic length. Small scale computer simulations demonstrate that the computational approach produces realistically looking results.

### 13.1 Introduction

Extraction of gas or oil from shale strata by hydraulic fracturing of oil and gas bearing rocks, aka “fracking,” is by now a well-established technology [2, 14, 29, 40, 45]. It has been developed gradually since 1947, under private funding except for some public funding during the last few years, granted after the viability had

---

Z.P. Bažant (✉)

McCormick Institute Professor and W.P. Murphy Professor of Civil and Mechanical Engineering and Materials Science, Northwestern University, 2145 Sheridan Road, CEE/A135, Evanston, IL 60208, USA  
e-mail: [z-bazant@northwestern.edu](mailto:z-bazant@northwestern.edu)

V.T. Chau

Graduate Research Assistant, Northwestern University, Evanston, IL, USA

© Springer International Publishing Switzerland 2016  
C. Jin, G. Cusatis (eds.), *New Frontiers in Oil and Gas Exploration*,  
DOI 10.1007/978-3-319-40124-9\_13

435

already been proven. Nevertheless, despite astonishing progress, the knowledge of the growth of the hydraulic crack system is still mostly empirical and no method exists for predicting the growth of an extensive system of branched hydraulic fractures which must develop in successful wells. The purpose of this chapter is to review the recent advances previously presented in full detail in [11] and [21].

### 13.2 Brief Overview of Fracking Technology

The gas bearing stratum of tight shale, typically about 3 km below the surface and 20–150 m in thickness [22, 44], is accessed by parallel horizontal boreholes, about 500 m apart (Fig. 13.1). They are drilled from a single drillpad in the direction of the minimum principal tectonic stress  $\sigma_h$ , whose magnitude is about 1/5 to 4/5 of the overburden stress [32]  $\sigma_g$ .

The horizontal boreholes used to be about 3 km long, but 11 km is now being attained. Each of them is subdivided into segments about 600 m long, each of which consists of about 5–10 fracturing stages. Each stage, typically 70 m long, is further subdivided into about 5–8 perforation clusters. In each cluster, about 14 m long, the steel casing (or pipe), of typical inner diameter 3.5 in. (77 mm) [28, 49], is perforated at 5–8 locations by detonating groups of shaped explosive charges (Fig. 13.1).

Powerful pumps on the surface drillpad inject the fracking fluid into the shale stratum. The fluid, about 99 % water, contains proppant (a fine sand needed to prevent crack closure), and contains various additives, particularly gellants, various acids or pH controlling ions. Each stage requires injection of several million gallons of water (which is equivalent to about 0.5–2 mm of rain over the area of the lease,  $3 \times 5$  to  $10 \text{ km}^2$ ). The flowback of water, representing about 15 % of the injected total, is very salty and highly contaminated with dissolved minerals. Strict controls are required to prevent its accidental release to the environment. Often, the water

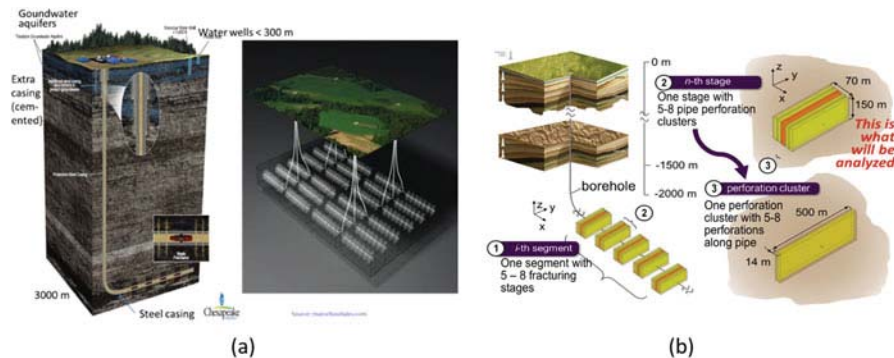


**Fig. 13.1** Main features of frac operations. (a) Overview of Frac Operations. (b) Main Features of Frac Operation

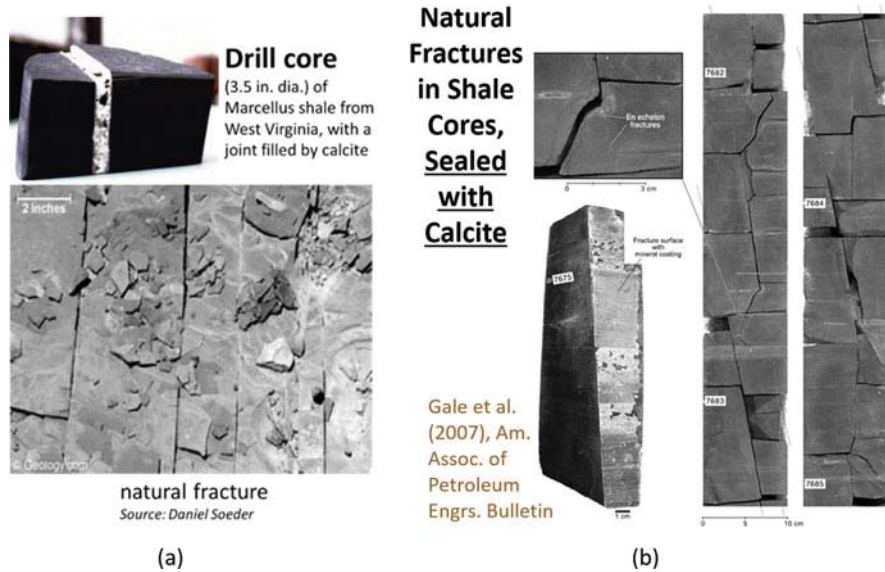


**Fig. 13.2** Vertical joints in Devonian Shale (Marcellus); (a) drilled cores, (b) surface outcrop

flowback is reinjected underground. Minimization and treatment of this flowback is an important goal of research.

Pumps, currently attaining at the surface level the pressure of about 25 MPa, push the fracking fluid through the perforations into the shale stratum. To begin with, the shale is intersected by a system of natural fractures or rock joints, nearly vertical, which are either tightly closed or filled by calcite or other minerals. They are typically 15–50 cm apart [29, 42] (Fig. 13.2). The shale is also intersected by numerous finer faults and inclined slip planes. The shale contains weak near-horizontal bedding planes with sub-millimeter spacing, which have higher permeability and higher concentration of kerogen filled nano-voids [36]. The first, large, hydraulically produced cracks must be roughly normal to the horizontal wellbore, since it is always drilled in the direction of the minimum tectonic stress. No horizontal cracks are expected to form since the overburden pressure exceeds the tectonic stresses.

Most of the gas in gas shale, mainly methane, is contained in kerogen-filled nanopores of diameters from 0.5 nm to about 10 nm [33, 34, 36]. Drilled cores brought to the surface (Fig. 13.2) reveal the total gas content of shale, and thus it is estimated that at most 15 %, and often as little as 5 %, of the gas content of the shale stratum gets extracted (percentages as high as 50 % have been rumored but probably are rare local aberrations).

### 13.3 Estimation of Hydraulic Crack Spacing from Gas Flow History Observed at Wellhead

According to reported measurement, the shale permeability,  $k$ , ranges from  $10^{-9}$  darcy to  $10^{-7}$  darcy, which is 10 to 1000 times lower than the typical permeability of concrete; e.g., [38]. The huge spread of the measured  $k$ -values reported in the literature [23, 36, 39, 46] is probably caused less by differences among locations and more by differences among the methods of measurement [3, 31]. These are transient methods based on the long-term decay of gas loss using: (1) a drilled core or (2) powderized shale, obtained by grinding the shale to particle size of about 0.5–0.85 mm.

The tests of the cores are dominated by diffusion along the kerogen-filled bedding layers in which the clay mineral platelets are oriented mainly horizontally, making the permeability higher than in the rest of shale. On the other hand, the powder test depends more on the compacted clay rock between the bedding layers in which the clay platelets do not have a preferential orientation. This feature reduces the permeability. Since the hydraulic cracks must be orthogonal to the bedding layers, the core test appears to be more relevant. The average permeability,  $10^{-8}$  darcy, has been considered in calculations.

#### 13.3.1 Diffusion of Gas from Shale into Hydraulic Cracks

To quantify the gas escape from the nano-voids into the nearest hydraulic cracks, we consider an idealized typical situation—one-dimensional gas diffusion in direction  $x$  into adjacent parallel cracks of spacing  $s$ , normal to  $x$  (Fig. 13.3). The Darcy law, given by the equation in Fig. 13.3b, is assumed to apply [1, 2]; and the condition of mass conservation appears below.  $t$  = time,  $v$  = velocity of gas,  $p$  = gas pressure,  $\phi$  = gas porosity,  $\mu$  = dynamic viscosity of the gas, and  $C_s$  = bulk compressibility of shale; and  $\rho$  = mass density of the gas. The gas closely follows the ideal gas equation, i.e.,  $p/\rho = RT = \text{const.}$ , which means that the gas compressibility is  $C_g = 1/p$ . Using  $p = \rho R T$  in the previous two equations, and noting that constant  $RT$  cancels out, one obtains, after some rearrangements. Because of nonlinear compressibility of gas, the diffusion equation is strongly nonlinear [13].

For a shale layer between two parallel cracks at  $x = 0$  and  $x = s$ , the flux of gas from the layer into the cracks at  $x = 0$  is given by the equation in Fig. 13.3b (middle left). This represents an interface condition for the flow of gas into the hydraulic crack system. With this interface condition, the diffusion equation is solved numerically by central finite differences in the spatial direction and explicitly by forward finite differences, while the time step  $\Delta t$  is lengthened as the flux decays, to the extent allowed by the limit of numerical stability.

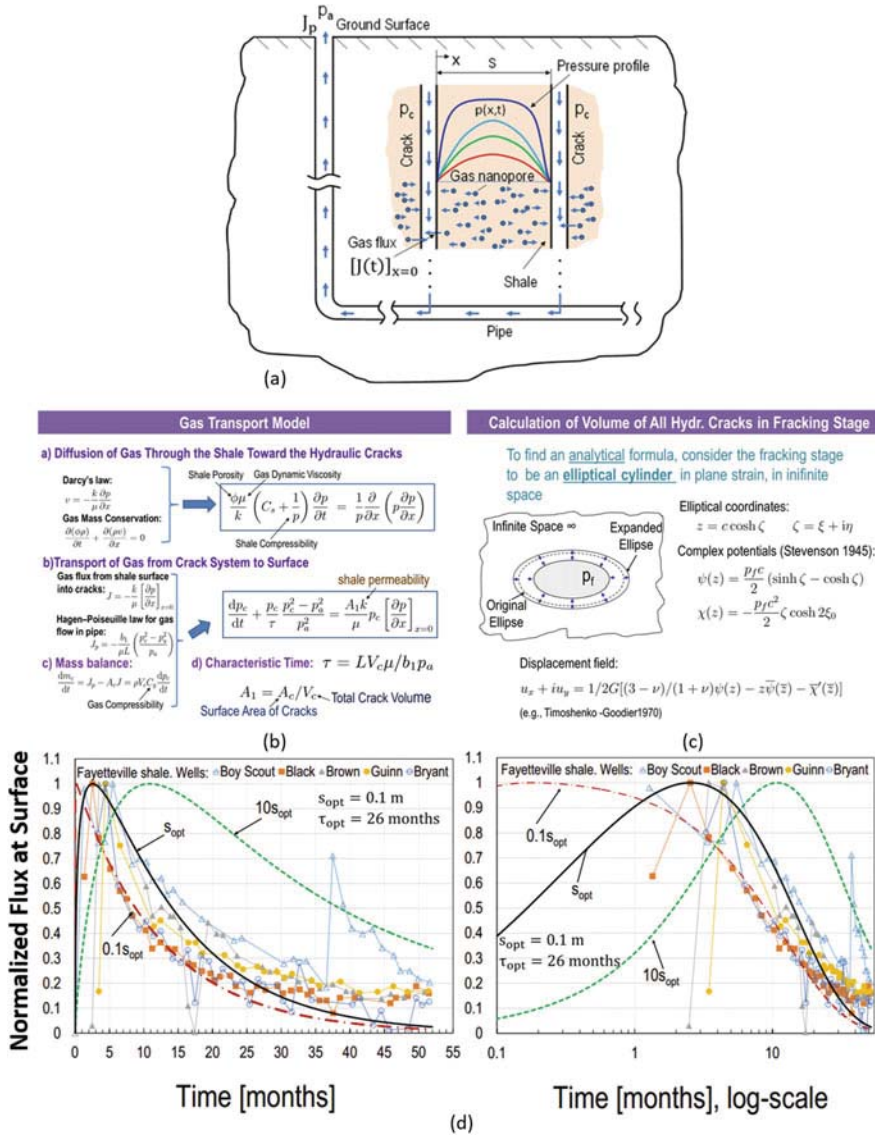


Fig. 13.3 Steps in estimating crack spacing from gas flow. (a) Schematic of Gas Transport from Shale to Surface. (b) Gas Transport Mathematical Model. (c) Calculation of Volume of All Hydraulic Cracks in Fracking Stage. (d) Effect of Crack Spacing on the Gas Flux Histories

### 13.3.2 Total Volume and Surface Area of Hydraulic Crack System

To relate the  $J$  to the flux of gas observed at the wellhead in the initial transient period about 1 month long, we need to estimate the total volume  $V_c$  and total surface area  $S_c$  of all the hydraulic cracks in a fracturing stage. Since at most only 15 % of the gas is currently getting extracted, we optimistically assume that the fracked shale volume is 15 % of the volume of a typical fracturing stage (70 m long, 150 m deep, and 500 m wide, Fig. 13.3c), which is  $V_{cyl} = 495,000 \text{ m}^3$

The pressure of fracking water generally does not exceed the overburden pressure. Therefore, all the cracks must be approximately vertical. They are assumed to consist of two approximately orthogonal systems of parallel cracks. There are two reasons for the orthogonality: (1) The rock joints, which are the preferred crack locations, are roughly orthogonal, and (2) equilibrium of a horizontal element bounded by four non-orthogonal vertical cracks would require transmission of shear stresses across the cracks, which is impossible if the cracks are fully open.

To make analytical estimates possible, we idealize the fracked zone as an elliptical cylinder with a vertical axis, height  $h$  and a generating horizontal ellipse of axes  $a$  and  $b$  (Fig. 13.3c), such that the cylinder volume,  $\pi a b h$ , be equal to  $V_{cyl}$ . The fractured rock inside the cylinder is under uniform pressure  $p$  equal to the fracking pressure, from which one can calculate the combined volume decrease of these rocks,  $\Delta V_{in}$  (see the inner ellipse in Fig. 13.3c). The total surface area of all cracks (each crack having two faces) is  $S_c = 4\pi abh/s$ .

Further one needs to calculate the enlargement of the area of the idealized ellipse considered as a pressurized hole in an infinite elastic plane (elastic modulus  $E = 37.5 \text{ GPa}$  and Poisson ratio  $\nu = 0.3$  in the planes of the bedding layers). The area increase  $\Delta A$  of the elliptical hole in infinite plane due to internal fracking pressure  $p_f$  was calculated using Stevenson's solution [48, 50] in complex variables, which was extended to obtain also the displacements. The main equations are shown in Fig. 13.3c), and in detail see [11] ( $p_f$  is here considered to be in excess of the average remote tectonic pressure  $p_{tectonic} = (\sigma_h + \sigma_H)/2 \approx 40 \text{ MPa}$ ). The area increase multiplied by cylinder height gives a crude estimate of the volume increase  $\Delta V_{out}$  due to compression of the surrounding shale mass. The total volume of the crack system of the fracking stage is  $V_c = \Delta V_{in} + \Delta V_{out}$ .

### 13.3.3 Flow of Gas from the Hydraulic Crack System to the Wellhead

To estimate the crack spacing, we need to figure out the rate of gas flow through the hydraulic cracks and through the horizontal and vertical pipes. Since the gas is mostly methane and methane does not dissolve in water, the gas must move as

bubbles, which start as microscopic but soon coalesce into big bubbles filling the crack width and the pipe diameter. In the hydraulic crack system, as well as in the horizontal and vertical pipes, the bubbles are driven by gas pressure gradient and move in turbulent flow. In the vertical pipe, the movement of gas bubbles is, additionally, also propelled gravitationally, by buoyancy. Detailed modeling of the movement of gas bubbles is quite involved, but for a crude estimate it suffices to use the Hagen–Poiseuille law for the flow of a compressible fluid in pipes, shown in Fig. 13.3b (bottom left) where  $J_p$  = flux of gas out of the fracked zone into the hydraulic crack system;  $p_c$  = inlet pressure = gas pressure at, approximately, the center of the fracked zone;  $p_a$  = atmospheric pressure = gas pressure at exit on the surface;  $L$  = distance of flow; and  $b_1$  = constant characterizing the resistance to gas flow through the hydraulic crack system and the horizontal and vertical sections of the pipe. The condition of mass balance is written for the entire volume of the hydraulic cracks (see Fig. 13.3b where  $dm_c/dt = J_p$  = rate of change of gas mass contained in all the opened hydraulic cracks, where  $p_c$  = average gas pressure in the crack system,  $C_g$  = gas compressibility,  $V_c$  = total volume of the opened hydraulic cracks,  $A_c$  = area of the surfaces of all opened hydraulic cracks = double of the total crack area,  $S_c$ ). Combining all the equations, one can obtain the final approximate equation for the decay of gas pressure  $p_c$  in the hydraulic crack system shown in Fig. 13.3b (bottom right), in which the most important parameter is the gas flux halftime  $\tau$ , giving approximately the time at which the gas flux decays to 20 % of its peak.

Now we are ready to make comparisons with the observed gas flux. Figure 13.3d shows the gas flux histories observed at five wells in Fayetteville shale in Arkansas (freely downloaded from the internet) [37]. The histories are plotted in actual time scale on the left and the logarithmic time scale on the right. They have two key features that must be matched by computations:

1. The halftime of flux decay,  $\tau$ ; and
2. The time to reach the peak flow,  $\tau_{\text{peak}}$ .

Matching these two times by numerical solution of the aforementioned equations has made it possible to estimate the crack spacing  $s$  [11]. The calculated history of gas flux giving the least-square optimum fit is shown in Fig. 13.3d by the solid curve. It corresponds to crack spacing

$$s_{\text{opt}} \approx 0.1 \text{ m} \quad (13.1)$$

and to halftime  $\tau_{\text{opt}} = 26$  months. To realize how credible this estimate is, see the curve for  $s = 1$  m and for  $s = 0.001$  m. Obviously there is no match at all (Fig. 13.3d). How well the time to peak gas flow is matched can better be seen in the logarithmic time scale in Fig. 13.3d right.

### 13.3.4 Long-Term Gas Flow as the Main Indicator of Crack Spacing

How big is the error in crack spacing,  $s$ , due to simplifications of the analysis of the gas flow from the hydraulic cracks to the wellhead? In fact, small. These simplifications can affect significantly only the time to peak flow,  $\tau_{\text{peak}}$ , but not the flux after a few years. In fact, even if the transmission of gas from the hydraulic cracks to the wellhead was considered immediate, the terminal part of the curves of the *relative* decay of the gas flow in Fig. 13.3d would hardly be affected.

The slope of the long-time descending curve in linear time, or the location of the steep descent in log-time (compare the descending solid and dashed curves in Fig. 13.3d) depends almost only on the crack spacing and thus on the permeability of shale, which can be directly measured (this is, of course, not true for the initial rising part of gas flow history which depends strongly on the delay of gas flow through the pipes; without this delay, the gas flow history would descend from the start). The reason is that, after approximately 1 year, the gas flow is declining very slowly and is close to a steady state. In a steady state, the rate of gas flow from the shale into the cracks would be exactly equal to the rate of gas flow at the wellhead.

Another reason why the crack spacing estimate of 0.1 m [11] ought to be quite reliable is that the halftime of the rate gas flow from the shale into the hydraulic cracks scales is approximately proportional to the *square* of crack spacing. If the crack spacing was 1 m, the half time,  $\tau$ , would increase from 26 to 2600 months, or 217 years, and if the crack spacing was 10 m, to 21,700 years. Were the cracks spaced at 1 cm, the halftime would decrease to 0.26 month or 7.6 days. The fact that all of these halftime values grossly disagree with experience reinforces the spacing estimate of 0.1 m.

The consequence of the crack spacing estimate of 0.1 m is that complete fracturing of one typical fracking stage would require creating about one million vertical cracks, in two orthogonal crack systems. Yet most previous studies have dealt with one hydraulic crack [2, 16, 24–26, 30, 35], and lately with five parallel (i.e., nonintersecting) cracks [15, 17–19]. These studies are valuable for clarifying the micromechanics of fracking, especially the complicated interaction of crack tip singularity with viscous flow near the singularity, and with capillary meniscus and surface adsorption of water near the singular crack tip. But they have little relevance for the overall fracking operation.

There is, nevertheless, one phenomenon which could alter the crack spacing estimate appreciably—the creep, which is in fact quite pronounced in shale. Its main consequence is that proppant particles (sand grains) must be getting gradually embedded into the walls of hydraulic cracks, thus causing that, with the lapse of time, the proppant can prevent crack closure only partly. The creep embedment must lead to a decrease of crack width and perhaps even to crack closure, thus reducing or even stopping the flow of gas. This might be one reason why refracking, with more proppant, helps. However, data on the creep of shale are scant at present and more testing is needed.

### 13.4 Evolution of a System of Parallel Hydraulic Cracks

#### 13.4.1 Hydrothermal Analogy

For the steady states of multiple hydraulic cracks, a previous study [11] pointed out a simple analogy with thermal cracks. Consider an elastic halfspace that is getting cooled from the surface (Fig. 13.4). If the temperature drop is high enough, parallel cooling cracks will form. The heat conduction produces a temperature field that decays from the surface as the error function.

First imagine that some external agency would apply on the crack surfaces a pressure that would close the cracks, and then glue them. Second, the agency would unglue the cracks. The ungluing is equivalent to applying opposite pressure on the crack surfaces; see Fig. 13.4 right. Since, for the glued cracks, the stress intensity factors  $K_c$  at the crack tips vanish, the solution of the crack system according to linear elastic fracture mechanics (LEFM) is, for the thermal cracks, the same as it is for the hydraulic cracks.

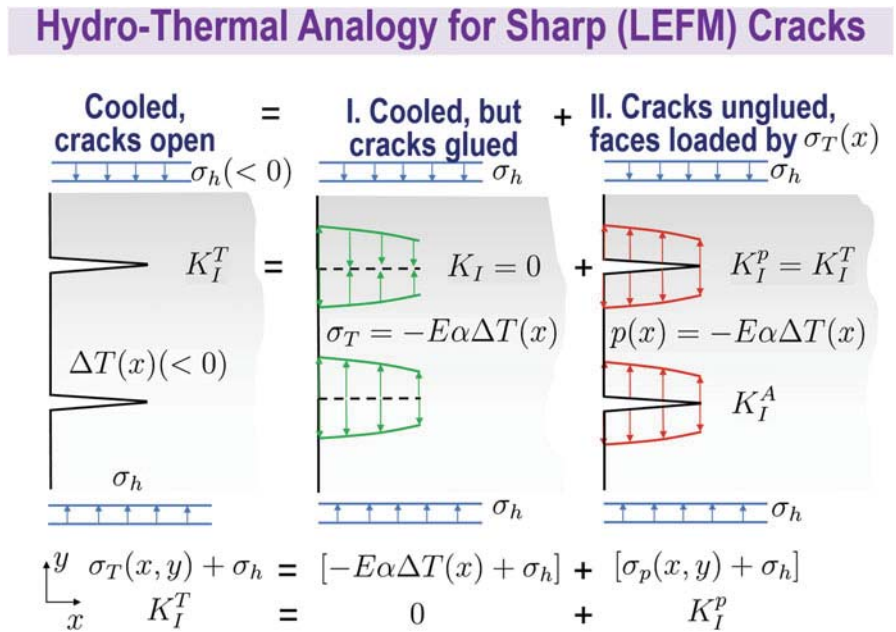


Fig. 13.4 Superposition leading to hydrothermal analogy

### 13.4.2 Review of Stability of Parallel Crack Systems

At the time of the first energy crisis in the mid 1970s, extraction of heat from hot dry rock located relatively close to the earth surface was studied. It was speculated that if a large vertical crack was created hydraulically from a borehole in hot granite (Fig. 13.5a), and if this crack was then intersected by another borehole, circulation of water could deliver enough steam to generate electricity. Success would have required the cooling to produce many closely spaced parallel cracks propagating laterally from the walls of the main crack. However, drilling into the ancient Valles Caldera in the Jemez Mountains of New Mexico gave a negative result, which was explained [7, 9] by analysis of the localization instability of parallel cooling cracks.

This negative result nevertheless provides today some useful information for the understanding of one aspect of fracking, particularly the stability of a parallel crack system (Fig. 13.5c) against localization. The stability can be assessed on the basis of the Helmholtz free energy,  $F$ , of a structure with interacting cracks of lengths  $a_1, a_2, \dots, a_N$  and fracture energy  $\Gamma$  for each crack (LEFM being assumed); see the top equation in Fig. 13.5c, in which  $U$  = strain energy of the elastic solid;  $p$  = control parameter, such as the depth of penetration  $D$  of the fluid pressure front into the halfspace, analogous to the cooling front.

In fracking as well as cooling, there are many possible fracture equilibrium solutions but, according to thermodynamics, the stable one is that which minimizes  $F$ . The equilibrium and stability of the crack system are, respectively, decided by the first and second variations [7], written at the bottom of Fig. 13.5c ( $i = 1, \dots, m$  are the cracks that are growing ( $\delta a_i > 0$ ) and dissipating fracture energy  $\Gamma$ ;  $i = m + 1, \dots, n$  are the cracks that are shortening ( $\delta a_i < 0$ ), for which the fracture energy is 0, and  $i = n + 1, \dots, N$  are the cracks that are immobile ( $\delta a_i = 0$ ), which occurs if the energy release rate  $-\partial U / \partial a_i$  is non-zero but less than critical. Equilibrium (or static) crack propagation requires vanishing of the first variation (which yield the standard crack propagation criterion. Fracture stability requires the matrix of the second variation  $\delta^2 F$  (Fig. 13.5c bottom) to be positive for all admissible variations  $\delta a_i$  [5, 7, 9, 41].

Consider that cooling or hydraulic cracks may develop alternating lengths  $a_i (i = 1, 2)$  although initially they are equal (Fig. 13.5b). The positive definiteness of the matrix of  $\delta^2 F$  was shown to be lost first by the vanishing of its determinant. But this indicates neither instability nor bifurcation because the corresponding eigenvector implies every other crack to shorten ( $\delta a_2 = -\delta a_1 \neq 0$ ), which is impossible since the energy release rates of all cracks are nonzero. After further crack advance, when the crack length becomes about  $1.5s$  to  $2s$ , the positive definiteness of the matrix of  $\delta^2 F$  is lost due to the vanishing of the first diagonal term while the corresponding eigenvector of  $\delta a_i$  is found to be admissible. This implies a stable bifurcation, in which the length of every other crack jumps ahead, while the remaining cracks unload and close. Thus the spacing of the leading cracks doubles, and their opening width  $w$  eventually does, too [7, 8, 41].

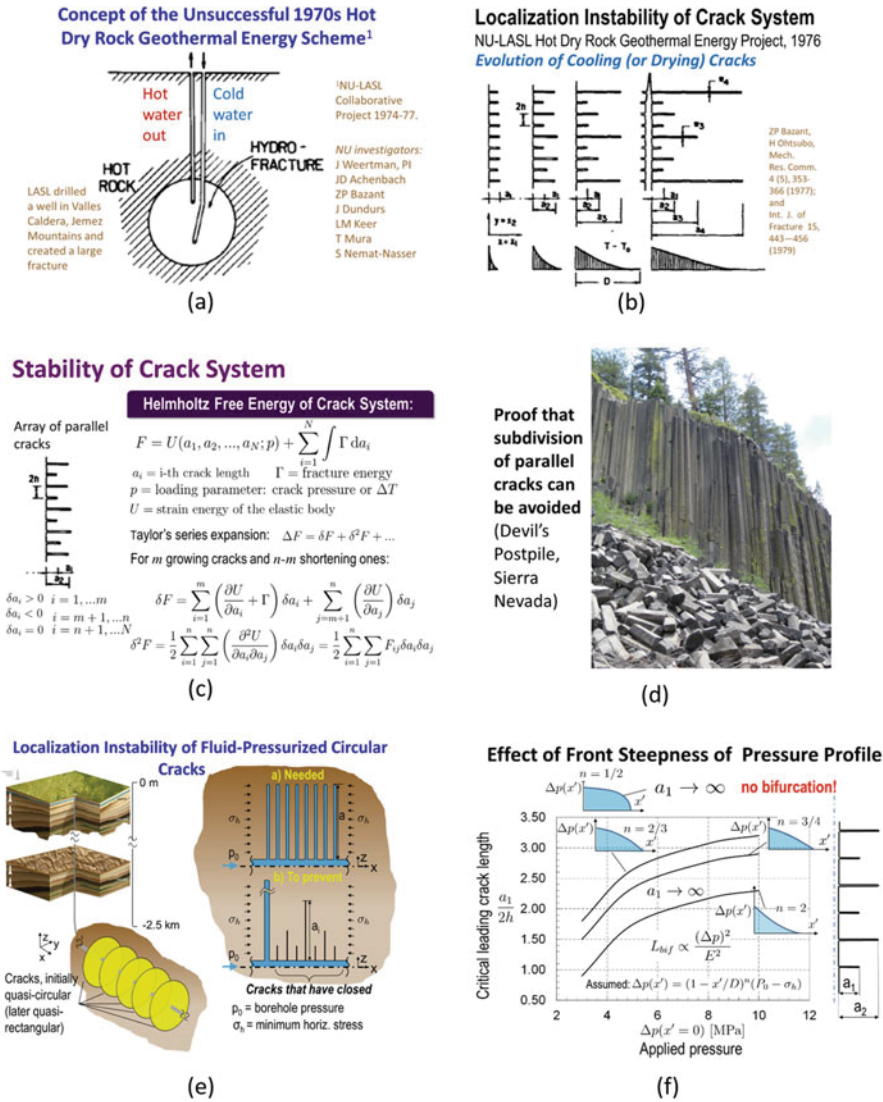


**Fig. 13.5** Bifurcations and localization instabilities of parallel crack system. (a) Concept of the Unsuccessful Hot Dry Rock Geothermal Energy Scheme. (b) Localization Instability of Geothermal Crack System in Hot Dry Rock. (c) Stability Analysis of Crack System. (d) Evidence of Parallel Cracks. (e) Localization Instability of Fluid-Pressurized Circular Cracks. (f) Effect of Front Steepness of Pressure Profile

The remaining leading cracks of doubled spacing  $2s$  eventually reach another bifurcation of the same kind, at which the spacing every other crack stops growing and gradually closes while the spacing of the open cracks doubles to  $4s$  (Fig. 13.5b). This doubling of crack spacing, in which the crack system localizes into fewer and fewer cracks, is periodically repeated as the pressure front (or cooling front)

advances (see also [5, Sect. 12.5]). The rate of gas flux into the leading cracks decreases approximately in inverse proportion to crack spacing  $s$ .

However, these bifurcation instabilities with cracking localization can be avoided. This is, for example, blatantly demonstrated by the photo of Devil's Postpile in Sierra Nevada (Fig. 13.5d) which shows the denuded side wall of a solidified ancient lava flow. Obviously, here the cracking localization was prevented by a complex thermal regime affected by latent heat of solidification and by circulation of water along the cracks.

For the present problem, it was found in 1979 [5, 12] that if the error-function profile is replaced by a profile with nearly uniform pressure and a steep drop at front, the parallel cracks can propagate at constant spacing, with no localizations into fewer cracks (Fig. 13.5f). The same behavior was recently demonstrated for parallel radially growing circular cracks (Fig. 13.5e [11]). Such behavior is, of course, desirable for the efficacy of fracking.

So we may conclude that the effect of temperature profile on fracture propagation is generally the same as that of a similar crack pressure profile. Thus the previous analysis of cooling cracks makes it possible to state, even without any calculations, that by achieving a sufficiently uniform crack pressure profile, with a sufficiently steep pressure front, the parallel cracks should not get localized and should propagate indefinitely, at constant spacing. This is what is needed to create densely spaced channels by which the shale gas could escape from the nanopores.

From the foregoing considerations it transpires that a nearly uniform pressure profile is one feature that should help the efficacy of fracking. To make the pressure along the cracks more uniform, a slower pumping rate is desirable. This observation, however, will have to be balanced against many other influencing factors. And, of course, for the 3D intersecting crack systems, and in presence of water diffusion into the pores, the problem of preventing localization of hydraulic cracks is much more complex and deserves further study.

### 13.5 Evolution of Two Orthogonal Systems of Hydraulic Cracks

Given that the spacing (Fig. 13.3) is about 0.1 m, the number of vertical near-orthogonal cracks in a typical fracking stage must be about a million. The hydraulic fracture system doubtless includes fractures running along preexisting rock joints [47, 52, 54]. Although the joints are usually filled by calcite, their tensile strength and fracture energy are certain to be smaller, probably much smaller, than those of shale. Hence, the hydraulic cracks must be expected to run along the rock joints whenever possible. That they do, is supported by the fact that the spacing of rock joints is on the order of 0.1 m, coinciding with our estimate of crack spacing.

An effective way to deal with a vast number of cracks is the crack band model [6, 20], in which the crack is smeared and represented as equivalent damage over

the finite element of a width equal to the crack band width. Compared to the cohesive crack model, an additional advantage is that atensorially enriched cohesive softening law, sensitive to compression stress parallel to the crack plane, can be used. The finite element size is taken equal to the crack spacing, about 0.1 m. This way, of course, the local stress and flow fields at crack tip cannot be captured, but the global evolution of crack system can. Even with this element size, about a billion finite elements would be needed to simulate the whole fracking stage, unless a method of coarse graining taking into account the global cracking localizations is developed.

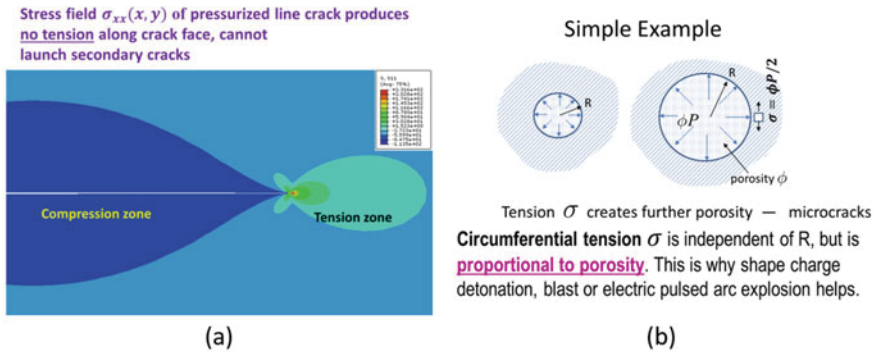
### ***13.5.1 Cracked Finite Elements for Crack Band Model***

The shale mass is subdivided into six-node cubic (hex) finite elements with linear shape functions (Fig. 13.7a). Each element contains two vertical, mutually orthogonal, cracks normal to the  $x_1$  and  $x_2$  axes, coinciding with the principal tectonic stresses  $T_1$  and  $T_2$  ( $x_1 \equiv x$ ,  $x_2 \equiv y$ ). The opening widths of the cracks normal to these stresses, denoted as  $h_1$  and  $h_2$ , respectively, govern the components of the vectors  $(q_1, q_3)$  and  $(q_2, q_3)$  of the flux vectors of water along these cracks,  $q_3$  being the vertical flux component. The water pressure,  $p$ , is considered to be uniform within each element, and since the cracks intersect, pressure  $p$  in each element must be the same in both intersecting cracks. Pressure  $p$ , of course, varies from one element to the next.

### ***13.5.2 Secondary Lateral Crack Initiation and the Necessity to Include Diffusion***

In the previous studies, the fracking water was assumed to flow only along the opened cracks, pressuring the crack walls. In this way, however, no secondary cracks would branch from the crack walls (V-shaped branching at the crack tip is possible only in dynamics, at crack speeds close to Rayleigh wave speed). The secondary cracks initiate if the horizontal normal stress,  $\sigma_{11}$ , parallel to the face of a vertical cracks is tensile and exceeds the strength limit,  $\sigma_0$ , of the cohesive crack or the crack band model [6, 10, 20]. However, according to LEFM, the stress field on the sides of a pressurized crack (Fig. 13.6a, b top left and bottom) is compressive. This can be shown not only by finite element analysis but also from Westergaard's complex variable solution (Fig. 13.6b bottom).

By contrast, if a spherical or wide ellipsoidal cavity is pressurized (Fig. 13.6b, c) [50, p. 395], a tensile tangential normal stress along the cavity wall is produced and can give rise to a crack. The same is true when the pores in a porous spherical or ellipsoidal cavity are pressurized, producing on the cavity walls an effective



**Diffusion in Pores is What Initiates Secondary Branched Crack**

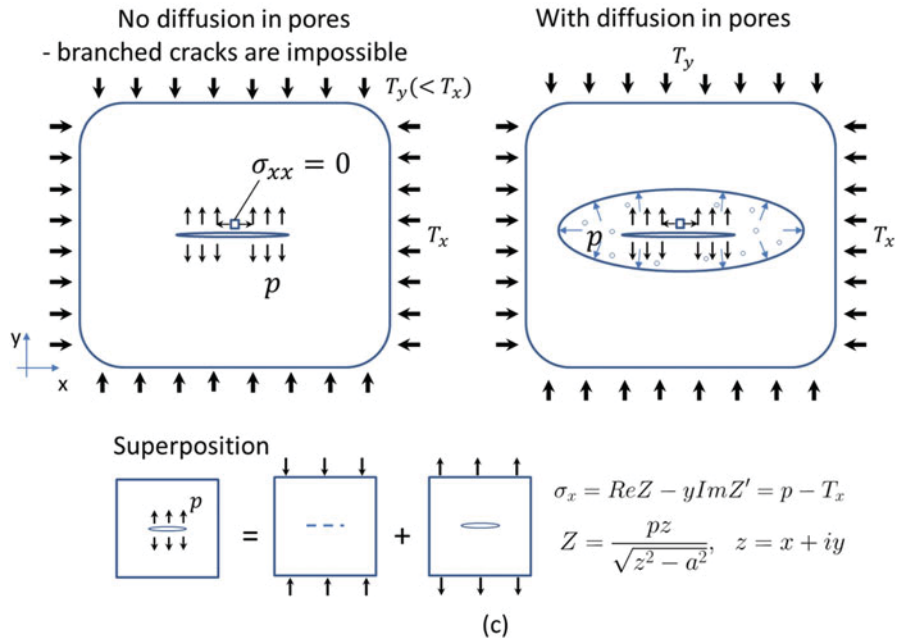


**Fig. 13.6** Engendering tension along the wall of crack or cavity. (a) Stress field  $\sigma_{xx}$  of pressurized crack. (b) Relationship of circumferential tension and porosity. (c) Diffusion in pores initiates secondary branched crack

pressure  $\phi p$  where  $p$  = pore pressure and  $\phi$  = porosity. So the mathematical model must include diffusion of water into the shale surrounding a hydraulic crack. Such diffusion would not be a realistic assumption for granite, for example, but for shale it is, because the typical nano-porosity of shale (e.g., Marcellus shale) is  $\phi = 9\%$ . This assumption is also supported by the fact that the fracking water leak-off is huge, as only about 15% of the water injected from the wellhead returns to the surface after the fracking ends.

Consequently, one must consider not only the Poiseuille (viscous) flow along the created hydraulic cracks, but also the Darcy diffusion through the pores and flaws in shale.

### 13.5.3 Water Flow Through Hydraulic Cracks and Pores

The flow along the hydraulically created cracks is assumed to follow the Reynolds equations of classical lubrication theory, which are based on the Poiseuille law for viscous flow; see Fig. 13.7a top left where  $q_1, q_2, q_3$  = flux vector components in the vertical  $(x_1, x_3)$  and  $(x_2, x_3)$  crack planes ( $x_1 \equiv x, x_2 \equiv y, x_3 \equiv z$ ). where  $\tilde{q}_1, [\tilde{q}_3]_{(x_1, x_3)}$  are the volumetric Poiseuille flow rates per unit cross-sectional area (dimension m/s) in plane  $(x_1, x_3)$ ; likewise  $[\tilde{q}_3]_{(x_2, x_3)}$  in plane  $(x_2, x_3)$ ;  $\tilde{P}$  = water pressure in the cracks;  $h_1, h_2$  = openings of the cracks in  $(x_2, x_3)$  and  $(x_1, x_3)$  planes (i.e., in  $x_1$  and  $x_2$  directions), and  $\mu'$  = effective viscosity of fracking water, which is affected by proppant and gellants. The diffusion of water (without proppants) through the pores of shale is governed by the Darcy law [13]; see Fig. 13.7a top right where  $k = 1, 2, 3$ ,  $\hat{q}_k$  =  $k$ th component of the vector of volumetric flow rate through the pores, per unit cross-sectional area (dimension m/s);  $\hat{P}$  = water pressure in the pores;  $\mu$  = water viscosity [1, 2] (taking into account the effect of gellants but not proppants), and  $\kappa_h, \kappa_v$  = permeabilities of porous shale along the horizontal bedding planes and in the vertical direction (dimension  $m^2$ ) [53], which are rather different;  $\kappa_v \ll \kappa_h$  [36, 46]. In computations  $\kappa_v$  is neglected. Adding the fluxes through the pores and through the cracks gives the equations in Fig. 13.7a (middle left). Water pressure  $P$  is, in the global model, common to the pores and the hydraulic cracks.

### 13.5.4 Combined Diffusion Through Shale Pores and Flow Along the Cracks

In the global model, the water pressures in the cracks and in the pores are considered to be locally the same within each finite or volume element. So the water mass conservation equation must be written for the combined mass of water in the pores and in the cracks. After introducing the Darcy and Poiseuille fluxes, the combined diffusion equation takes the form in Fig. 13.7a (bottom left); in which  $l$  = side of cubic element;  $h_1, h_2$  = opening widths of cracks normal to axes  $x, y$  (or  $x_1, x_2$ );  $\kappa_h, \kappa_v$  = permeabilities of shale in horizontal and vertical directions (the vertical permeability, normal to the bedding layers, is much smaller).

Although water is considered as incompressible in previous studies, it is in fact about 10–30 times more compressible than rocks. The compressibility of water is considered by the equation for mass density  $\rho$  of water in Fig. 13.7a (bottom left), where  $C_f$  = compressibility of water with proppant,  $\rho_0$  = mass density at reference pressure, and  $p_0$  = reference pressure taken as gravity pressure of water at the depth

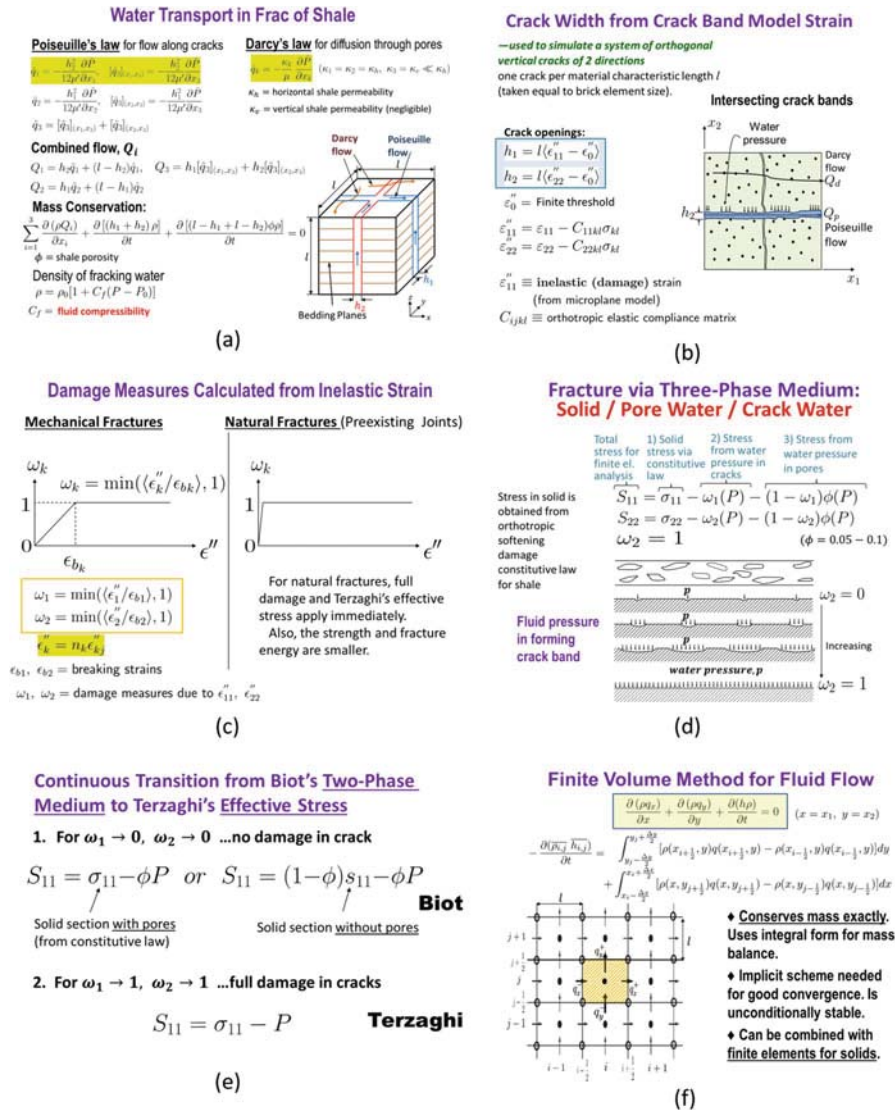


**Fig. 13.7** Mathematical modeling for finite element and finite volume analysis. (a) Water Transport in Frac of Shale. (b) Crack Width from Crack Band Model Strain. (c) Damage Measures Calculated from Inelastic Strain. (d) Fracture via Three-Phase Medium: Solid, Pore Water and Fracturing Water. (e) Continuous Transition from Biot's Two-Phase Medium to Terzaghi's Effective Stress. (f) Finite Volume Method for Fluid Flow

of shale layer before fracturing. Because the crack width is negligible compared to crack spacing, water compressibility is not important for overall deformations of fracked shale mass, but it matters for the pressure changes in water controlling the flow rates.

### 13.5.5 Crack Opening Corresponding to Smeared Damage Strain in Crack Band Model

Three potential, mutually orthogonal (or orthorhombic) cracks must be introduced in one finite element. Horizontal cracks are excluded because the vertical overburden pressure (about 80 MPa) generally exceeds the pressure of the fracking water ( $\leq 70$  MPa). The crack band width is taken equal to the material characteristic length  $l$ , which is equal to the crack band width or to the element size, and is defined as the minimum possible spacing of stable parallel cracks (note that  $l$  must be distinguished from Irwin's material length, which depends on material strength and fracture energy and characterizes the length, rather than width, of the fracture process zone).

The crack openings,  $h_i$  ( $i = 1, 2$ ), which control the rate of water flow, are, in the crack band model, calculated from the continuum damage strain  $\varepsilon''_{11}$  or  $\varepsilon''_{22}$  across the crack band, which is obtained from strains  $\varepsilon_{11}$  and  $\varepsilon_{22}$  calculated from the softening constitutive law; see Fig. 13.7b where  $n$  = empirical exponent; subscripts 1 and 2 refer to Cartesian coordinates  $x_1, x_2$  in the horizontal plane;  $\varepsilon''_{11}$  = inelastic (or damage) strain, and  $C_{ijkl}$  = orthotropic elastic compliance matrix of the shale ( $i, j, k = 1, 2, 3$ ). The constitutive law for softening damage of the solid (i.e., the shale), i.e.,  $\sigma = f(\varepsilon)$  must also be orthotropic (this law is another challenge which still awaits proper resolution based on triaxial test data);  $\sigma, \varepsilon$  are the stress and strain tensors with Cartesian components  $\sigma_{ij}$  and  $\varepsilon_{ij}$ ; and  $f$  is the tensorial function defining the constitutive law.

The distributed microcracking damage is characterized by transversely isotropic damage parameters,  $\omega_1$  and  $\omega_2$ , considered to be functions of the inelastic parts of strains,  $\varepsilon''_{11}$  and  $\varepsilon''_{22}$ . where  $\varepsilon_{b1}, \varepsilon_{b2}$  = specified breaking strain limits (Fig. 13.7c left). For the cracks in intact shale, they were taken as  $10^{-5}$  and, for the cracks along the preexisting cemented joints, as  $10^{-7}$ . The joints, whose volume is assumed to be 0, behave as potential cohesive cracks with reduced strength and reduced fracture energy.

### 13.5.6 Pore Pressure Effect on Stresses in the Shale

The shale with its cracks and pores is treated as a generalization of both Biot's two-phase medium and Terzaghi's effective stress concept [53]. Three phases may be discerned: (1) the solid shale, of volume fraction  $(1 - \omega_1)\phi$ , (2) the cracks, of a near-zero volume fraction, and (3) the pores of a significant volume fraction,  $\phi$ . Since no horizontal cracks exist, the equilibrium of the three phases leads to the equations in Fig. 13.7d where  $\phi$  = natural porosity of shale;  $\omega_1, \omega_2$  = additional porosities for the resultants of fluid pressure in  $x_1$  and  $x_2$  directions (Fig. 13.7d bottom); and  $S_{ij}$  = total stress tensor in the solid-fluid system, which are required by finite element analysis to calculate the nodal forces.

There are three contributions to the total stress tensor: (1)  $\sigma_{ij}$  is the stress tensor in the solid including the natural pores, which is calculated from the constitutive law of shale; (2)  $\omega_1 p, \omega_2 p$  are the cross-section resultants of water pressure in the cohesive (i.e., bridged) hydraulic cracks; and (3)  $(1 - \omega_1)\phi p$  and  $(1 - \omega_2)\phi p$  are the cross-section resultants of the pore water pressure. Alternatively, we could also write  $\sigma_{11} = (1 - \phi)s_{11}$  where  $s_{11}$  = stress resultant from cross section of solid without the natural pores and preexisting microcracks, whereas  $\sigma_{11}$  = stress that is spread out over the full cross section of solid including the pores (but excluding the hydraulic cracks). Using  $\sigma_{11}$  instead of  $s_{11}$  is preferable because  $\sigma_{11}$  is the stress directly measured in material tests.

Note that if there are no cracks with damage, i.e.,  $\omega_1 = \omega_2 = 0$ , the equations from Fig. 13.7e reduce to case 1 in Fig. 13.7e, which characterizes Biot's two-phase medium. In the opposite case of complete damage, i.e., if  $\omega_1 = \omega_2 = 1$  (with no bridges across the crack), the same equations in Fig. 13.7e reduce to case 2 in Fig. 13.7e, which gives the classical Terzaghi's effective stress. So we see that the present three-phase medium represents a continuous transition between these two classical (and historically disputed) concepts of soil mechanics.

### 13.5.7 Numerical Prediction of Evolutions of Hydraulic Crack System

The solid is discretized by finite elements, but this is not the best way for the fluid part of the system. The fluid is better treated by the finite element method [27, 43, 51], which has the advantage that the mass balance of the fluid is enforced exactly (Fig. 13.8a top). This is important if the front of the water infiltration zone is sharp. To combine both methods, the fluid flow elements overlap the finite elements for stress analysis as seen in Fig. 13.8a.

First, to study the behavior of mathematical model, we analyze the fracking of a 2D horizontal square slice of shale mass of unit height and size  $5 \text{ m} \times 5 \text{ m}$  [21], with the discretization shown in Fig. 13.8a. At each boundary node, we introduce elastic springs that approximately characterize the resistance of the surrounding infinite medium to horizontal expansion. The boundary is, for simplicity, considered impermeable to fluid flow, which means that the simulations are not realistic after the pressurized cracks approach the boundary. The overburden pressure is 80 MPa, corresponding to the depth of 3 km, and the tectonic stresses are  $\sigma_h = 30 \text{ MPa}$  and  $\sigma_H = 40 \text{ MPa}$ . The horizontal wellbore is considered to run at the bottom of the square in Fig. 13.8b–f. The fracking water first enters conical holes in shale thought to be about 0.5 m deep. These holes are created by explosions of a cluster of three shaped charges, which perforate the high-strength steel pipe. The proppants in water are assumed to suffice to prevent any closing of previously created cracks. The pressure history of water at inlet is a given function of time but here is considered as constant, equal to 70 MPa [21].

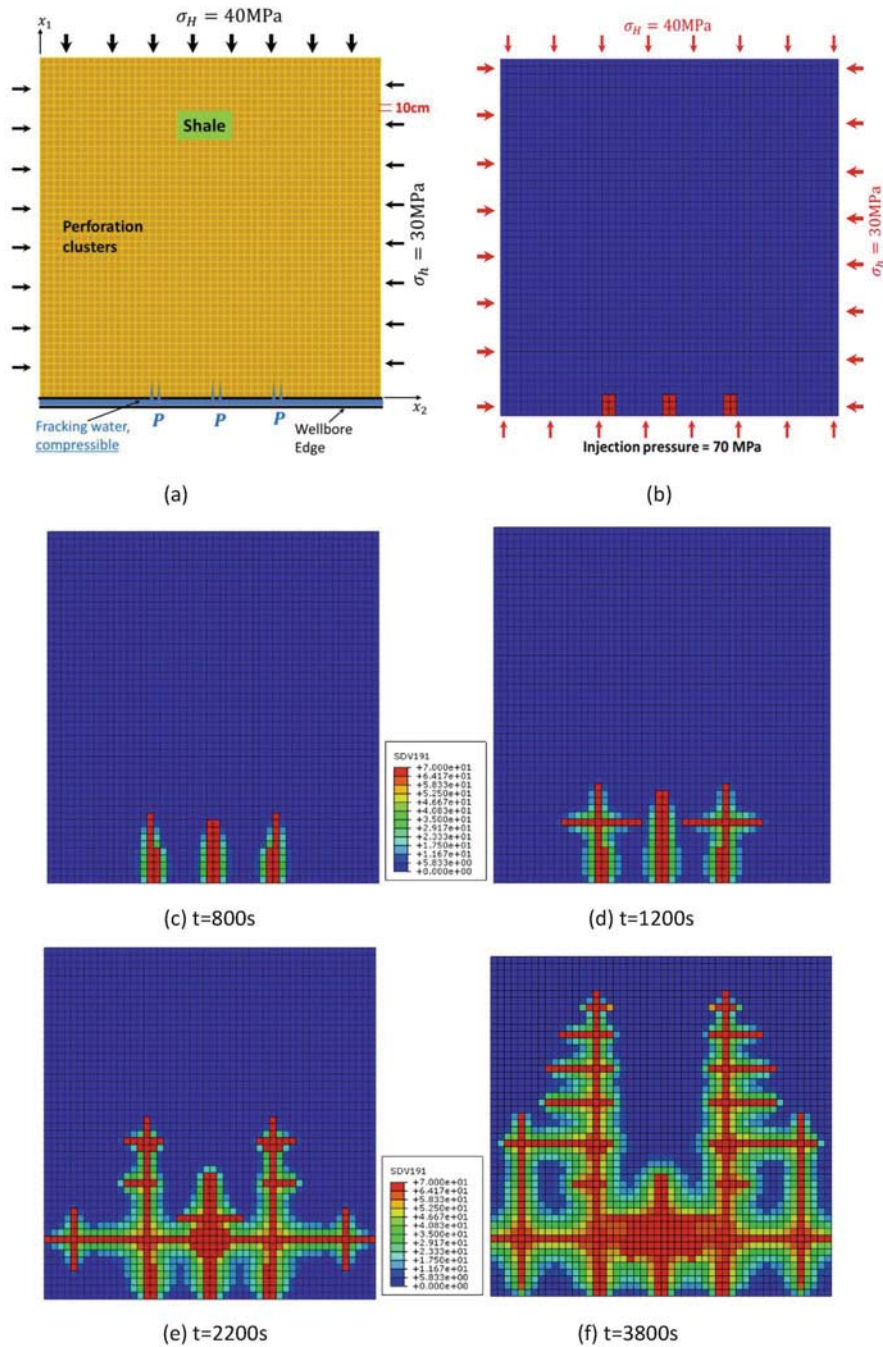


**Fig. 13.8** Demonstration of computed evolution of high pressure zones in 2D hydraulic crack system in shale *without* rock joints. (a) 2D Hydraulic Fracture Model without pre-existing rock joints. (b) Pressure Field at initial. (c) Pressure Field at time  $t = 800\text{s}$ . (d) Pressure Field at time  $t = 1200\text{s}$ . (e) Pressure Field at time  $t = 2200\text{s}$ . (f) Pressure Field at time  $t = 3800\text{s}$

The mechanical behavior of shale, which is isotropic in the horizontal plane, is described by a microplane model with postpeak softening, representing an adaptation to shale of the microplane model for concrete [4]. The embedment creep of proppant grains is not yet included in this simulation, whose duration is a few hours. The porosity of shale is  $\phi = 0.09$ , and the water viscosity is  $8.9 \times 10^{-4}$  Pa s. The tensile strength and fracture energy of shale are here considered to be  $\sigma_0 = 4.17$  MPa and  $G_f = 0.7$  N/mm in the intact shale, but 3.62 MPa and 0.5 N/mm for cracks running along rock joints (because of overburden and tectonic stresses, these values are higher than those measured in the laboratory).

Two cases have been analyzed (for details, see [21]): (1) All the cracks running through intact shale, and (2) 50 % of cracks running in preexisting joints, whose locations were predefined randomly. Figure 13.8b–f shows the subsequent zones of high pressure for the case of no preexisting joints, and Fig. 13.9 the same for the case of preexisting joints. The finite elements with the highest pressure reveal the locations of open hydraulic cracks. Figure 13.10 from another simulation shows one snapshot from the evolution of hydraulic crack width. The crack width is shown approximately proportional to line thickness and the greatest line width shown corresponds to the width of 10 mm.

Three-dimensional simulations, which are computationally far more demanding, have been demonstrated [21] for a smaller domain—a cubic block of shale with the side of only 0.9 m, shown in Fig. 13.11a. Here only one inlet of water from the horizontal wellbore is considered. All the other parameters are the same. Three subsequent snapshots of the pressure patterns [21] are shown on horizontal and vertical cuts of the block along the planes of symmetry, as shown in Fig. 13.11b, c.

## 13.6 Closing Comments

The present review of recent researches demonstrates how global fracture analysis with the crack band model, combined with water flow both through hydraulic cracks and through the pores of shale, can be used to simulate the growth of a large system of closely spaced branched hydraulic cracks in shale. Such simulations should allow studying the control parameters that maximize the area of hydraulic cracks and lead to fracking of the largest possible volume of shale with sufficiently close crack spacing. A powerful supercomputer will be needed to scale the analysis to the entire fracking stage.

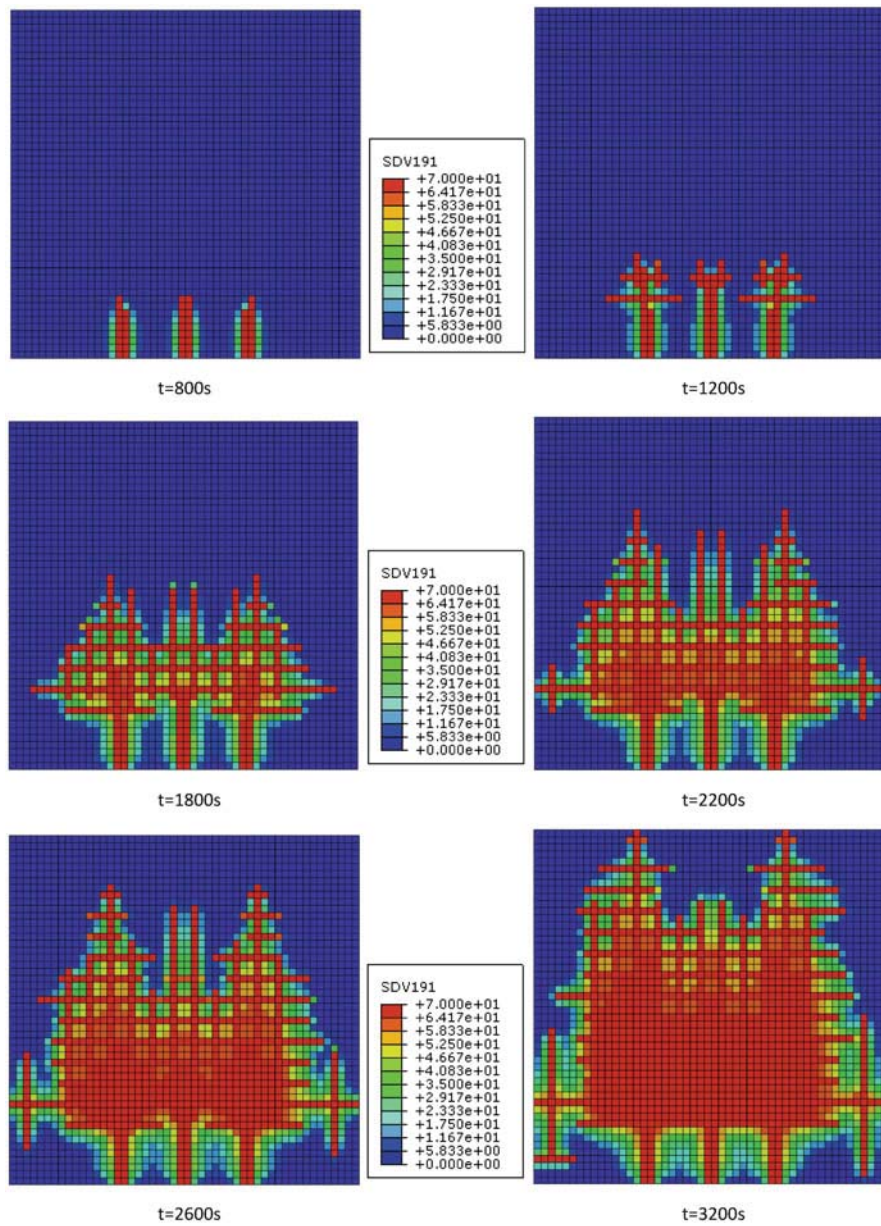


**Fig. 13.9** Demonstration of computed evolution of high pressure zones 2D hydraulic crack system in shale *with* rock joints

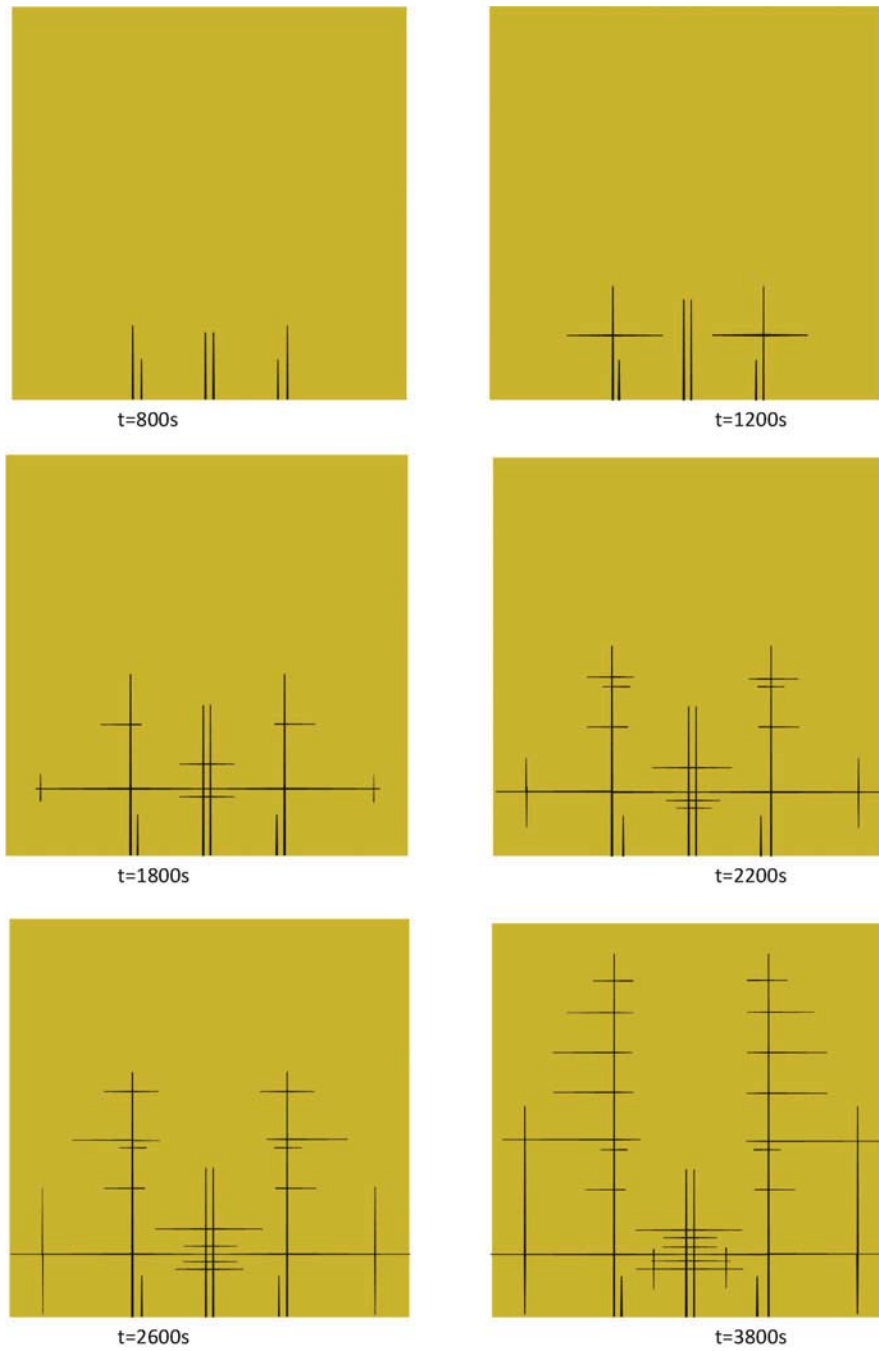


**Fig. 13.10** Demonstration of computed evolution of crack pattern

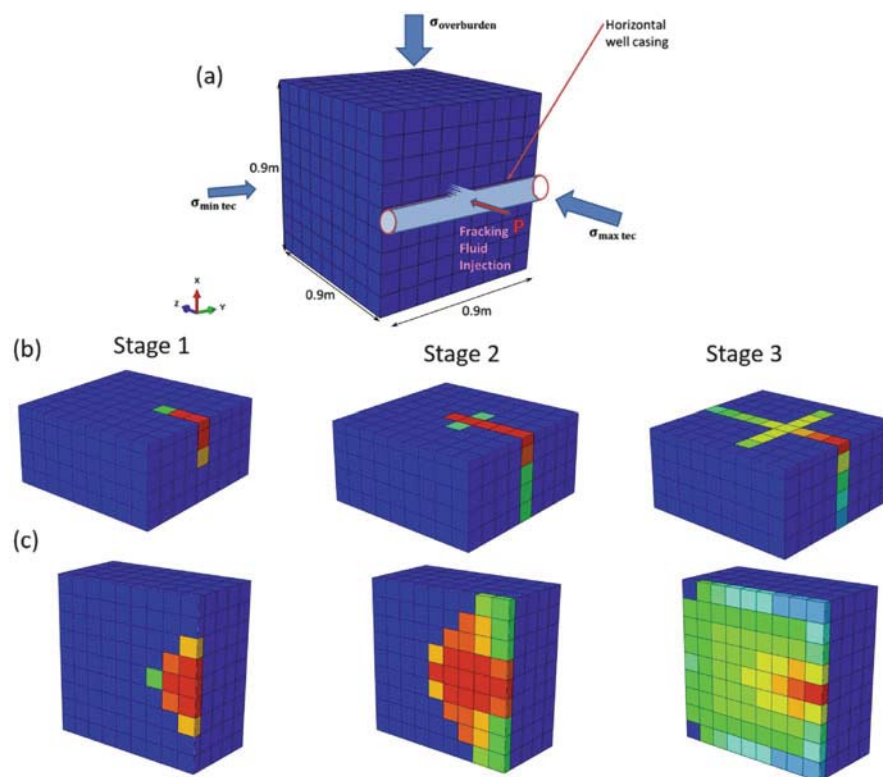


**Fig. 13.11** Computed evolution of high pressure zones of 3D hydraulic crack system in a cubic block of shale. (a) 3D Hydraulic Fracture Model. (b) Pressure Field in YZ Cross Section at Different Time Interval. (c) Pressure Field in XZ Cross Section at Different Time Interval

**Acknowledgements** Financial support from the U.S. Department of Energy through subcontract No. 37008 of Northwestern University with Los Alamos National Laboratory is gratefully acknowledged. Ramifications of fracturing analysis from concrete to shale were partially supported by ARO grant W911NF-15-101240 to Northwestern University.

## References

1. Adachi, J., Siebrits, E., Peirce, A., & Desroches, J. (2007). Computer simulation of hydraulic fractures. *International Journal of Rock Mechanics and Mining Sciences*, 44(5), 739–757.
2. Adachi, J. I., & Detournay, E. (2008). Plane strain propagation of a hydraulic fracture in a permeable rock. *Engineering Fracture Mechanics*, 75, 4666–4694.
3. American Petroleum Institute. (1998). Recommended Practices for Core Analysis. API RP40.
4. Bažant, Z. P., Caner, F. C., Adley, M. D., & Akers, S. A. (2000). Microplane model M4 for concrete: I. Formulation with work-conjugate deviatoric stress. *Journal of Engineering Mechanics ASCE*, 126(9), 944–953.

5. Bažant, Z. P., & Cedolin, L. (1991). *Stability of structures: Elastic, inelastic, fracture and damage theories*. New York: Oxford University Press (also 2nd ed. Dover Publ. 2003, 3rd ed. World Scientific 2010).
6. Bažant, Z. P., & Oh, B. H. (1983). Crack band theory for fracture of concrete. *Materials and Structures*, 16, 155–177.
7. Bažant, Z. P., & Ohtsubo, H. (1977). Stability conditions for propagation of a system of cracks in a brittle solid. *Mechanics Research Communications*, 4(5), 353–366.
8. Bažant, Z. P., & Ohtsubo, H. (1978). Geothermal heat extraction by water circulation through a large crack in dry hot rock mass. *International Journal for Numerical and Analytical Methods in Geomechanics*, 2(4), 317–327.
9. Bažant, Z. P., Ohtsubo, R., & Aoh, K. (1979). Stability and post-critical growth of a system of cooling and shrinkage cracks. *International Journal of Fracture*, 15, 443–456.
10. Bažant, Z. P., & Planas, J. (1998). *Fracture and size effect in concrete and other quasibrittle material*. Boca Raton: CRC Press.
11. Bažant, Z. P., Salviato, M., Chau, V. T., Viswanathan, H., & Zubelewicz, A. (2014). Why fracking works. *ASME Journal of Applied Mechanics*, 81(Oct.), 101010-1–101010-10.
12. Bažant, Z. P., & Wahab, A. B. (1979). Instability and spacing of cooling or shrinkage cracks. *ASCE Journal of Engineering Mechanics*, 105, 873–889.
13. Bear, J. (1988). *Dynamics of fluids in porous media*. Mineola, NY: Dover Publications, ISBN 0486656756.
14. Beckwith, R. (2010). Hydraulic fracturing: The fuss, the facts, the future. *Journal of Petroleum Technology*, 63(12), 34–41.
15. Bunger, A. (2013). Analysis of the power input needed to propagate multiple hydraulic fractures. *International Journal of Solids and Structures*, 50. doi:12.1016/j.ijsolstr.2013.01.004.
16. Bunger, A., Detournay, E., & Garagash, D. (2005). Toughness-dominated hydraulic fracture with leak-off. *International Journal of Fracture*, 134(02), 175–190.
17. Bunger, A., Jeffrey, R. G., & Zhang, X. (2014). Constraints on simultaneous growth of hydraulic fractures from multiple perforation clusters in horizontal wells. *SPE Journal*, 19 (04), 608–620.
18. Bunger, A., & Pierce, A. (2014). Numerical simulation of simultaneous growth of multiple fracturing interacting hydraulic fractures from horizontal wells. In *Proceedings of ASCE Shale Energy Conference*, Pittsburgh, PA.
19. Bunger, A. P., & Cardella, D. J. (2015). Spatial distribution of production in a Marcellus Shale well: Evidence for hydraulic fracture stress interaction. *Journal of Petroleum Science and Engineering*, 133, 162–166.
20. Červenka, J., Bažant, Z.P., & Wierer, M. (2005). Equivalent localization element for crack band approach to mesh-sensitivity in microplane model. *International Journal for Numerical Methods in Engineering*, 62(5), 700–726.
21. Chau, V. T., Bažant, Z. P. & Su, Y. (2016). Growth model of large branched 3D hydraulic system in gas or oil shale. *Philosophical Transactions*. Accepted.
22. Cipolla, C. L., Mayerhofer, M. J., & Warpinski, N. R. (2009). Fracture design considerations in horizontal wells drilled in unconventional gas reservoirs. In *SPE Hydraulic Fracturing Technology Conference, 19–21 January, Texas*.
23. Cui, X., Bustin A. M. M., & Bustin R. M. (2009). Measurements of gas permeability and diffusivity of tight reservoir rocks: Different approaches and their applications. *Geofluids*, 9, 208–223.
24. Detournay, E. (2004). Propagation regimes of fluid-driven fractures in impermeable rocks. *International Journal of Geomechanics*, 4, 35. doi:10.1061/(ASCE)1532-3641(2004)4:1(35).
25. Detournay, E. (2016). Mechanics of hydraulic fractures. *Annual Review of Fluid Mechanics*, 48(1), 311–339.
26. Detournay, E., & Peirce, A. (2014). On the moving boundary conditions for a hydraulic fracture. *International Journal of Engineering Science*, 84, 147–155.

27. Eymard, R., Gallouet, T. R., & Herbin, R. (2000). The finite volume method. In P. G. Ciarlet & J. L. Lions (Eds.), *Handbook of numerical analysis* (Vol. VII, pp. 713–1020). Amsterdam: North-Holland
28. Gale, J. F. W. (2002). Specifying lengths of horizontal wells in fractured reservoirs. *SPE Reservoir Evaluation & Engineering*, 78600, 266–272.
29. Gale, J. F. W., Reed, R. M., & Holder, J. (2007). Natural fractures in the Barnett shale and their importance for fracture treatments. *American Association of Petroleum Geologists Memoirs*, 91(4), 603–622.
30. Garagash, D., & Detournay, E. (2000). The tip region of a fluid-driven fracture in an elastic medium. *Journal of Applied Mechanics*, 67(1), 183–192.
31. Guidry, K., Luffel D., & Curtis J. (1995). Development of laboratory and petrophysical techniques for evaluating shale reservoirs - final technical report, Gas Shale Project Area, Restech, Inc., GRI Contract No. 5086-213-1390.
32. Haifeng, Z., Hang, L. Guohua C., Yawei, L., Jun, S., & Peng, R. (2013). New insight into mechanisms of fracture network generation in shale gas reservoir. *Journal of Petroleum Science and Engineering*, 110, 193–198.
33. Javadpour, F. (2009). Nanopores and apparent permeability of gas flow in mudrocks (shales and siltstones). *Journal of Canadian Petroleum Technology*, 48, 16–21.
34. Javadpour, F., Fisher, D., & Unsworth, M. (2007). Nanoscale gas flow in shale gas sediments. *Journal of Canadian Petroleum Technology*, 46, 55–61.
35. Lecampion, B. (2009). An extended finite element method for hydraulic fracture problems. *Communications in Numerical Methods in Engineering*, 25(2), 121–133.
36. Louck, R.G., Reed, R.M., Ruppel, S.C., & Jarvie, D.M. (2009). Morphology, genesis, and distribution of nanometer-scale pores in siliceous mudstones of the Mississippian Barnett shale. *Journal of Sedimentary Research*, 79, 848–861.
37. Mason, J. E. (2011). Well production profiles assess Fayetteville shale gas potential. *Oil & Gas Journal*, 109(11), 76–76.
38. Maurel, O., Reess, T., Matallah, M., de Ferron, A., Chen, W., La Borderie, C., et al. (2010). Electrohydraulic shock wave generation as a means to increase intrinsic permeability of mortar. *Cement and Concrete Research*, 40, 1631–1638.
39. Metwally, Y. M., & Sondergeld C. H. (2010). Measuring low permeabilities of gas-sands and shales using a pressure transmission technique. *International Journal of Rock Mechanics and Mining*, 48, 1135–1144.
40. Montgomery, C. T., & Smith, M. B. (2010). Hydraulic fracturing: History of an enduring technology. *Journal of Petroleum Technology*, 63(12), 26–32.
41. Nemat-Nasser, S., Keer, L. M., & Parihar, K. S. (1976). Unstable growth of thermally induced interacting cracks in Brittle solids. *International Journal of Solids and Structures* 14, 409–430.
42. Olson, J. E. (2004). Predicting fracture swarms: The influence of subcritical crack growth and the crack-tip process zone on joint spacing in rock. *Journal of the Geological Society of London*, 231, 73–87.
43. Patankar, S. V. (1980). *Numerical heat transfer and fluid flow*. New York: Hemisphere Publishing Corporation.
44. Rijken, P., & Cooke, M. L. (2001). Role of shale thickness on vertical connectivity of fractures: Application of crack-bridging theory to the Austin Chalk, Texas. *Tectonophysics*, 337, 117–133.
45. Society of Petroleum Engineers. (2010). *Legends of Hydraulic Fracturing (CDROM)*, ISBN:978-1-55563-298-4.
46. Soeder, D. J. (1988). Porosity and permeability of eastern Devonian gas shale. *SPE Formation Evaluation*, 3, 116–124.
47. Song, W., Jinzhou, Z., & Yongming, L. (2014). Hydraulic fracturing simulation of complex fractures growth in naturally fractured shale gas reservoir. *Arabian Journal for Science and Engineering*, 39(10), 7411–7419.

48. Stevenson, A. C. (1945). Complex potentials in two-dimensional elasticity. *Proceedings of the Royal Society of London A: Mathematical, Physical and Engineering Sciences* (Vol. 184, No. 997, pp. 129–179). The Royal Society.
49. Tang, Y., Tang, X., & Wang, G. Y. (2011). Summary of hydraulic fracturing technology in shale gas development. *Geological Bulletin of China*, 30, 393–399.
50. Timoshenko, S., & Goodier, J. N. (1970). *Theory of elasticity*. New York: McGraw Hill.
51. Versteeg, H., & Malalasekera, W. (2007). *An introduction to computational fluid dynamics: The finite volume method*. New York: Pearson Education Limited.
52. Weng, X. (2015). Modeling of complex hydraulic fractures in naturally fractured formation. *Journal of Unconventional Oil and Gas Resources*, 9, 114–135.
53. Zoback, M. D. (2007). *Reservoir geomechanics*. Cambridge: Cambridge University Press.
54. Zou, Y., Zhang, S., Ma, X., Zhou, T., & Zeng, B. (2016). Numerical investigation of hydraulic fracture network propagation in naturally fractured shale formations. *Journal of Structural Geology*, 84, 1–13.